Millimeter-Wave Imaging Using a Rotating Dynamic Antenna Array and Noise Illumination

Daniel Chen, *Graduate Student Member, IEEE*, Stavros Vakalis, *Graduate Student Member, IEEE*, and Jeffrey A. Nanzer, *Senior Member, IEEE*

***Abstract*—We present a novel approach to millimeter-wave imaging that combines a new dynamic antenna array concept with active illumination by means of noise signals and interferometric image formation. The concept is based on a sparse linear array of receiving antennas that is dynamically rotated about its centroid, combined with three noise transmitters that illuminate the scene. Cross-correlations of the scattered signals received by individual array elements provide spatial frequency samples of the scene, from which the scene can be reconstructed via inverse Fourier transform. As the spatial frequency sampled by an antenna pair is dependent on the antenna baseline vector, dynamic rotation of the linear array generates sampling curves in the spatial frequency domain, providing a denser sampling function and a more accurate scene reconstruction. While traditional static interferometric imaging arrays utilize nearly an order of magnitude fewer antenna elements than phased arrays, our dynamic array concept relies only on a sparse linear array, further reducing the number of hardware elements required. We discuss the design of a 38-GHz dynamic antenna array imaging system and present measurements of multiple reflecting objects.**

***Index Terms*—Dynamic antenna array, interferometric imaging, millimeter-wave imaging, radar imaging, sparse arrays, spatial frequency**

I. Introduction

MILLIMETER-WAVE imaging systems have the ability to sense through many materials, including fog, smoke, clouds, clothing, baggage, and certain building materials [1], [2], providing imaging capabilities where other sensing modalities, such as optical [3] or infrared [4], are challenged. Millimeter-wave technologies are also becoming more ubiquitous, reliable, and low-cost. For these reasons, microwave and millimeter-wave technologies are being increasingly used for a remote sensing and imaging applications [5]–[10]. Regardless of the types of scenes being measured by the microwave and millimeter-wave system, adequate representation of the measured scenes must exhibit high quality to allow further processing such as object recognition on the surface of earth, or the detection of hidden contraband [11]–[14].

The constraints of millimeter-wave imagers, particularly on those designed for imaging at a distance, often manifest themselves in both the hardware and algorithm domains. Phased arrays and focal plane arrays entail significant hardware requirements due in large part to the number of transmitting and receiving channels with their associated millimeter-wave hardware. Computational imagers can reduce the hardware burden but require significant processing to form images [15]–[17]. Interferometric imaging provides a mechanism for image formation with far less hardware than phased arrays, with such imagers implemented with an order of magnitude fewer elements than traditional arrays require [18]–[24]. While using antenna arrays that are physically sparse, these systems nonetheless form high-resolution images by generating very dense sampling functions in the spatial frequency domain via pair-wise cross-correlating the outputs of the elements in the array. The scene is recovered through an inverse Fourier transform of the sampled spatial frequency information. However, because the image formation relies on spatio-temporal incoherence of the signals received from the scene, interferometric imagers have traditionally been passive systems for detecting thermal radiation, thus requiring very high-gain receivers, long integration times, and wide bandwidth to detect the low power thermal signals. The bandwidth places a further constraint since each receiver output is usually digitized separately for element-level processing.

We present a new approach to millimeter-wave imaging that combines a dynamic antenna array with interferometric processing and active noise transmission. Using a sparse linear array with spatio-temporal dynamics, a dense spatial frequency sampling function can be obtained with even fewer hardware elements than typical two-dimensional interferometric imagers. While previous work has shown that dynamic antennas can capture scene information without image formation [25]–[27], in this work we expand on the dynamic array concept to implement full image reconstruction. We also overcome the sensitivity and bandwidth limitations of passive interferometric imagers by applying a recently developed active incoherent millimeter-wave (AIM) technique, where noise transmitters illuminate the scene, which mimics thermal radiation but provides orders of magnitude more received power than thermal radiation [28]–[30]. In contrast to mechanically or electronically steered systems, which typically form images by scanning, in our approach each cross-correlation sample captures information from the entire scene, thus the image can be formed using the initial measurements with coarse resolution. As the linear antenna array rotates and the spatial frequency sampling becomes denser, the image quality improves [31]–[33]. Furthermore, since the unambiguous field of view is inversely dependent on the spatial frequency sampling interval, dynamic arrays can obtain a wide field of view by synthesizing closely-spaced spatial frequency samples through

Manuscript received 2021.

This material is based in part upon work supported by the National Science Foundation under grant number 1708820 and grant number 1751655. *(Corresponding author: Jeffrey A. Nanzer)*

The authors are with the Department of Electrical and Computer Engineering, Michigan State University, East Lansing, MI 48824 USA (email: {chendan7, vakaliss, nanzer}@msu.edu).

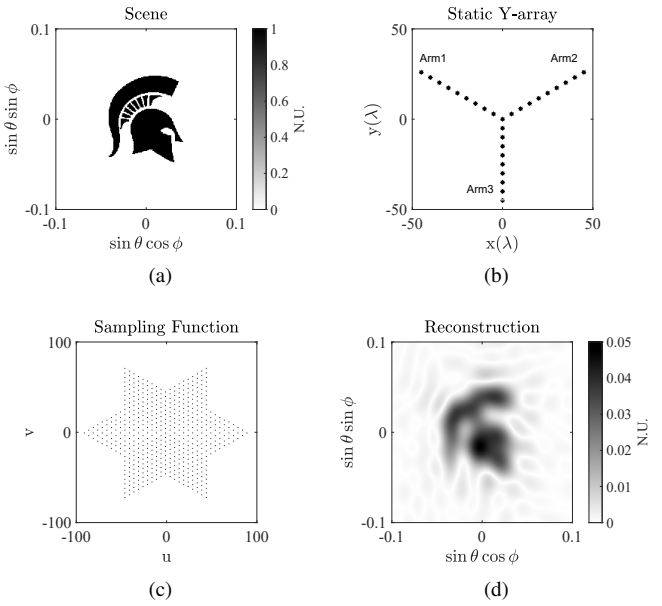

Fig. 1. Interferometric imaging example of a sparse array configuration and Fourier-domain processing to reconstruct images. (a) An example scene of the Michigan State University Spartan helmet. (b) Y-arrays are commonly used in interferometric imaging. This example uses a 28-element array with nine antennas on each of the three arms and one antenna at the center with inter-element spacing of 5λ which yields a maximum baseline separation of 95λ. (c) Corresponding spatial frequency domain sampling function defined by the pair-wise baseline separations relative to the wavelength of the array layout. (d) Interferometric imaging reconstruction via the 28-element Y-array.

small antenna dynamics without necessitating closely spaced hardware [2], [18]. We demonstrate image formation with an experimental 38-GHz dynamic antenna millimeter-wave imaging system. We synthesize a sparse linear array via translation motion of two antenna elements, which is equivalent to a sparse linear array since the signals are spatio-temporally incoherent.

II. Active Fourier Domain Imaging Using Transmission of Noise Signals

Interferometric imaging is a sparse antenna array technique that co-processes the signals received at pairs of receiving antennas to synthesize a larger aperture [18], [34]. Common formations of the interferometric array are the Mills Cross array, the T-array, and the Y-array [2]. Signals captured by the interferometer receivers can be grouped into two categories: radiation intrinsically produced by the scene, or those reflected off from the scene that are due to actively transmitting sources which are spatio-temporally uncorrelated and can either be internal or external to the sensing system. Systems relying on the former are commonly known as passive interferometers [34]–[38]. System leveraging active transmission are known as active interferometers [28]–[30]. Both interferometric techniques have been found in various applications such as contraband detection and space-borne remote sensing. The signals received by the receiving array may be either radiated by the scene itself in the form of thermal radiation or may be scattered off a scene illuminated by an active system. The received signals represent an intensity profile of the scene, given by $I(\alpha, \beta)$, where $\alpha = \sin\theta\cos\phi$ and $\beta = \sin\theta\sin\phi$ are the direction cosines described in (1). The cross-correlation of received signals due to combination of antenna pairs in an interferometric array generates samples of the Fourier transform of the scene, called the visibility $V(u, v)$, where u and v are the two-dimensional spatial frequencies. The Van Cittert-Zernike theorem gives the relationship between the visibility and the spatial intensity, which is given by [18], [39]

$$V(u,v) = \iint_{-\infty}^{+\infty} I(\alpha,\beta) e^{j2\pi(u\alpha+v\beta)} d\alpha d\beta. \tag{1}$$

The interferometric array measures only a subset of the visibility information, depending on the number of spatial frequency samples acquired by the array. The sampled visibility is the product of the scene visibility and the sampling function $S(u, v)$, thus a reconstruction of the scene visibility $I_r(\alpha, \beta)$ can be acquired through an inverse Fourier transform of the sampled visibility through

$$I_r(\alpha,\beta) = \iint_{-\infty}^{+\infty} V(u,v) S(u,v) e^{-j2\pi(u\alpha+v\beta)} du dv. \tag{2}$$

For a sparse interferometric array that comprises multiple antenna elements, the cross-correlation of the received signals within each antenna pair represents a unique sample of the visibility that is determined by their baseline separation, D. In the case of a 2D spatial Fourier space, the visibility is the result of cross-correlating information received at the antenna locations distributed in the x and y dimensions such that $u = D_x/\lambda$ rad^{-1} and $v = D_y/\lambda$ rad^{-1}. The quantities D_x and D_y are the projected baselines in the x and y dimensions for a given antenna pair and $\lambda = c/f$ is the wavelength of the received radiation. Thus, while the above formulation assumes a continuous sampling function, in practice the visibility is sampled discretely, such that the sampling function can be represented as

$$S(u,v) = \sum_{n}^{N} \sum_{m}^{M} \delta(u-u_n)\delta(v-v_m), \tag{3}$$

where $\delta(\cdot)$ is the Dirac delta function and $N \times M$ is the total number of samples that the sparse interferometric array acquires. However, since some baselines may be repeated, it is not necessarily equivalent to the number of spatial frequency samples acquired. The reconstructed scene intensity is then found by

$$I_r(\alpha,\beta) = \sum_{n}^{N} \sum_{m}^{M} V(u_n,v_m) e^{-j2\pi(u_n\alpha+v_m\beta)}. \tag{4}$$

An example illustrating the interferometric imaging process using a conventional 28-element Y-array with inter-element spacing of 5λ that yields a maximum baseline separation of 95λ is shown in Fig. 1. The image reconstruction simulations took place using MATLAB.

To accurately reconstruct the scene intensity via (4), the radiation emitted by or scattered off the scene must be spatially and temporally incoherent. Intrinsic thermal radiation

naturally satisfies this requirement but yields very low power at millimeter-wave frequencies, necessitating high-gain receivers. Active transmission imparts higher signal power, thus standard gain receivers can be used, however the transmitted radiation must be incoherent at the scene. We have previously explored the requirements on transmit incoherence for active incoherent imaging systems and have demonstrated the feasibility of using a small set of noise transmitters to illuminate the scene with sufficient incoherence to form images using Fourier domain processing [40]–[44]; we have furthermore shown that communications signals also support sufficient incoherence to generate imagery in the same manner [30], [45]. Operation of the system in the near-field of the array furthermore can improve the incoherence of the illumination due to the spherical wavefronts from each transmitter impinging differently on the scene [46]. Generally, the maximum dimension of the receiving array of AIM imaging systems is equivalent or shorter than that of the transmit array, however the scene is often still in the near field of the receiving array. Nonetheless, when the scene is near broadside within the field of view of the imager, the phase errors on the receiver are typically minimal compared to the far-field approximation [47], [48].

III. Dynamic Antenna Array for Spatial Fourier-Domain Imaging

For an interferometric imaging system, the total number of unique spatial frequency samples impacts the quality of reconstructed image: more unique samples leads to more spatial frequency information, yielding a higher quality image. However, the number of samples for a conventional static array is usually limited by $N \times M$ from (4). In contrast, additional receiving channels are not required if a given array can be efficiently reconfigured through array dynamics in order to acquire additional unique spatial frequency samples. One possible implementation is to implement a dynamic metasurface aperture which is tuned to achieve various array configuration. In this work we propose a different type of array dynamics where a linear antenna array with rotational dynamics is implemented to dramatically increase the number of spatial frequency information that can be captured with a minimal amount of millimeter-wave hardware. We combine the dynamic array concept with AIM imaging to significantly improve the sensitivity compared to passive imagers, thus supporting the use of fast antenna array dynamics. The dynamic antenna (Fig. 2) consists of a linear antenna array that is rotated about the array's centroid, which may or may not coincide with an element in the array. As the antenna array rotates, the projected baselines of a given antenna pair D_x and D_y vary, leading to a sampling function that covers a range of spatial frequencies. With sufficient rotational dynamics and only a small number of elements in the linear array, dense sampling functions can be synthesized. While we consider a uniform linear antenna array, the number of antenna elements may be further reduced with the use of a minimum-redundancy array [49].

In a static antenna array the spatial frequency sampling function is determined by the pair-wise baseline vectors of the antennas in the array layout. The sampling function for a rotational dynamic array with L elements can be given in terms of the antenna baselines D_l and the set of K rotation angles $\gamma(k)$ by

$$u_{lk} = D_l \sin\left(\gamma(k)\right), \tag{5}$$

and

$$v_{lk} = D_l \cos\left(\gamma(k)\right), \tag{6}$$

where the discrete rotation angles are given in terms of the initial angle of the array γ_0, the rotation rate γ_r, and the integration time for each sample τ by

$$\gamma(k) = \gamma_0 + \gamma_r k\tau. \tag{7}$$

The dynamic spatial frequency sampling function is thus given by

$$S_D(u,v) = \sum_{l=0}^{L-1} \sum_{k=0}^{K-1} \delta\left(u - u_{lk}\right) \delta\left(v - v_{lk}\right). \tag{8}$$

Note that the rotation direction is determined by the sign of the rotation rate r.

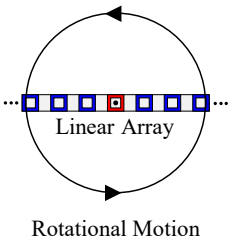

Fig. 2. Illustration of the proposed dynamic antenna array based on a sparse linear array with rotational dynamics with regard to the centroid of the array. The center antenna of the array is shown in red and antennas on either side from the center are shown in blue. Via a simple rotation of the array, a significant increase in the density of the spatial frequency sampling function can be obtained with a minimal set of hardware.

The dynamic antenna imaging concept is shown in Fig. 3 for a uniform linear array with $L = 9$ and an inter-element spacing of 12λ yielding a maximum dimension of 96λ which is comparable to the 95λ from the 28-element Y-array from Fig. 1(b). All simulations and plots took place using MATLAB. Figs. 3(a)-(d) show the physical locations of the elements during the rotation for four time instances at the start of the measurement, at half-way through, three-quarters through, and at the completion of the measurement. The rotation traces out concentric circles, synthesizing a nested circular array. Figs. 3(e)-(h) show the progression of the sampling function at the same times using (8). Because the array is uniformly spaced, the resulting sampling function is similarly in the form of nested circles. Note that due to the symmetry of the array and the sampling function, the array rotates only over a 180° angle to form the full sampling function. Figs. 3(i)-(l) show the reconstruction of the Spartan helmet from Fig. 1(a) using (8) then (4) for the four instances, demonstrating the improvement in image formation throughout the dynamic progression of the antenna array. At the initial measurement, since the array is a simple linear array, the reconstruction results only in variations within one dimension. Half-way through the measurement, the

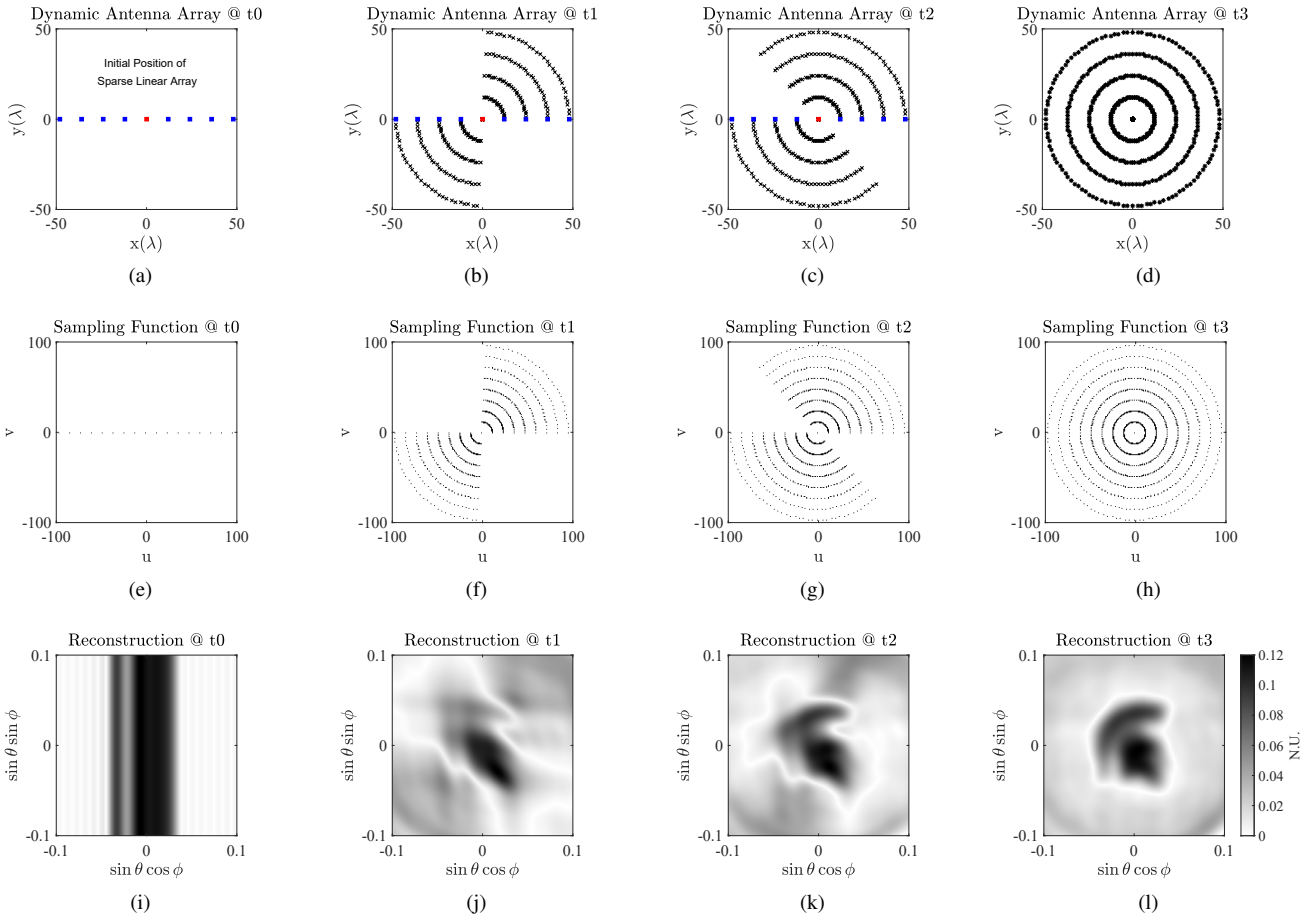

Fig. 3. Illustration of a dynamic antenna array based on a nine-element sparse linear array with counter-clockwise rotational motion for interferometric imaging at four instances. Each column of plots (from top to bottom) comprises the dynamic antenna array, the corresponding sampling function, and the reconstruction at the same instance. To evaluate against the conventional static interferometric array example shown in Fig. 1, the same scene (Fig. 1(a)) is used for reconstruction. The dynamic rotation progresses sequentially from the left to the right showing the progression of the elapsed dynamic antenna array formation from (a) initial position of the nine-element sparse linear array with the center antenna shown in red and the remaining in blue; to (b) elapsed dynamic antenna array formation after one quarter rotation; to (c) elapsed dynamic antenna array formation after three quarters rotation; and to (d) the total elapsed dynamic antenna array formation after a 180° rotation. Similarly, the progression of the synthesized sampling function associated with the elapsed dynamic antenna array formation are shown. (e) The starting sampling function, corresponding to a sparse linear array, and the successive synthesized sampling function (f), (g), and (h), the final synthesized sampling function; and the progression of (i) reconstructed image from nine-element sparse linear array without rotational dynamics to (l) final reconstruction, which is comparable to the result from the conventional static Y-array as shown in Fig. 1(d).

two-dimensional image begins to take form, with increasing refinement throughout the dynamic array progression. The final reconstruction results in an image similar to that of the Y-array (Fig. 1). However, the dynamic array image in this case is formed with less than $1/3$ the number of antenna elements comparing to the Y-array. TABLE I gives a comparison between the static 28-element Y-array and the 9-element dynamic antenna array, showing the number of unique uv samples, the peak signal-to-noise ratio (PSNR), and the structural similarity index metric (SSIM) [50] between the reconstructed images and Fig. 1(a). It can be seen that while the dynamic array has fewer receivers, more spatial frequency samples are obtained, yielding a higher PSNR, and a SSIM value closer to 1 which indicates better image quality.

The minimum observation time for a complete measurement is dependent on the per-sample integration time and the number of samples by $T = k\tau$ (see (7)). While typical passive interferometric imagers necessitate integration times

TABLE I
COMPARISON BETWEEN STATIC Y ARRAY AND DYNAMIC ARRAY

	Static	**Dynamic**
Example	Fig. 1(d)	Fig. 3(l)
Number of Receivers	28	9
Unique uv Sample Points	541	1405
PSNR (dB(N.U.))	3.39	11.72
SSIM	0.45	0.72

of up to seconds, AIM imaging enables image reconstruction with significantly less integration time to obtain equivalent sensitivities: recent work has demonstrated the ability to form images at more than 650 frames per second [51]. Thus, with noise transmission, the integration time τ can be made small relative to the dynamics of the environment in many situations, such as in contraband detection. While the integration time in [51] was only 64 μs, with system latencies the total measurement time per frame was 1.469 ms. To characterize the maximum potential rotation rate of the dynamic array, we

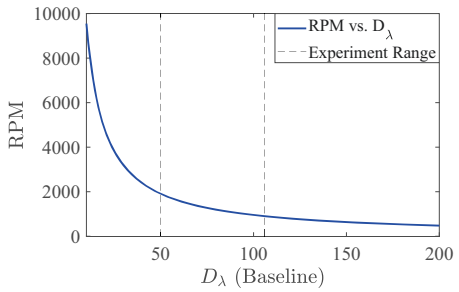

Fig. 4. Maximum rotational speed versus baseline formed by the two receiving antennas based on a spatial frequency grid (uv-plane) increment of 1 cycles $\cdot$ rad^{-1} and a minimum dwell time per grid of 10 ms. The two dashed-black lines indicate the range of baselines achieved by the implemented experimental setup.

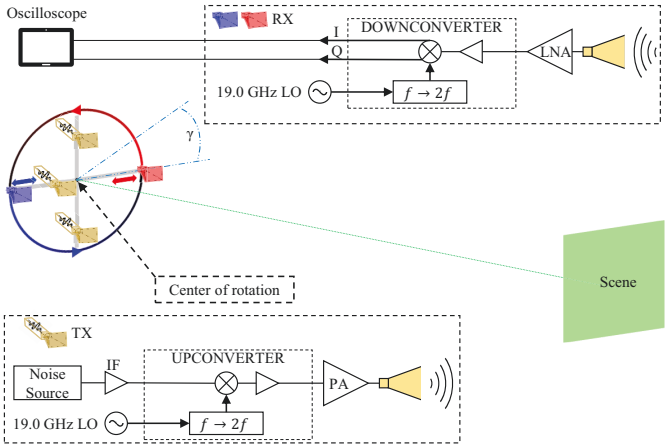

Fig. 5. System architecture of the 38-GHz experimental dynamic antenna array system. To demonstrate the dynamic array concept with the available hardware, two receiving antennas (i.e., blue and red horn antennas) were adjusted length-wise (indicated by blue and red double arrows) to enable baselines of a spare linear array to be synthesized. Simple rotational dynamics in the counter-clockwise direction were implemented in order to dynamically synthesize sampling function in the spatial Fourier domain. The three noise transmitting sources (i.e., yellow horn antennas) were rotated along with the receiving antennas to ensure co-polarization.

consider a spatial frequency grid in the uv-plane in increment of 1 cycles $\cdot$ rad^{-1} and an integration time of $\tau = 10$ ms, an integration time well above that demonstrated in prior AIM experimental work. The dynamics of the array must therefore be such that the dwell time within a spatial frequency pixel is not less than the integration time, otherwise the received signal information will be spread across multiple spatial frequency pixels. The maximum dwell time is dependent on the rotation rate of the antenna and the maximum antenna baseline $D_{\max}$, and the number of unique spatial frequency grids/samples is given by $2\pi D_\lambda$. The equivalent rotation rate of the array in rotations per minute (RPM) for a dwell time of 10 ms is shown in Fig. 4 as a function of the maximum baseline up to 200λ. Also, the ranges of baselines used in the experimental setup are shown, which are described in the next section. The rotation rate is near 1000 RPM and above for all cases, indicating that the temporal dynamics of the antenna array are not a limiting factor for image formation. Furthermore, these rates support implementation for applications where the environmental dynamics are sufficiently slower such that the scene can be considered static during the dynamic array rotation, such as contraband detection, remote sensing, and monitoring of manufacturing processes.

IV. System Architecture and Experimental Implementation

A 38-GHz experimental system was implemented to demonstrate the dynamic antenna array operation and to show proof-of-concept reconstructions of simple reflecting targets. To facilitate the experiments with existing hardware, the linear receiving array was synthesized by using only two receiver antennas placed on a rotating structure. Three noise transmitters were used to implement AIM processing with short integration times.

The dynamic array system architecture is shown in Fig. 5. The three noise transmitting sources marked by the yellow horn antennas are fixed on a cross-shaped rotatable frame rail. The blue and red horn antennas represent the two receiving antennas where both have side-way adjustment to enable various baselines to be synthesized to form an equivalent sparse uniform linear array. Furthermore, the receiving antennas are positioned on the same frame rail to share the same rotational motion with the transmitting antennas. This is important as co-polarization between the transmitting and receiving antennas can be maintained to ensure that maximum receiving signals are available at all times [52]. Polarization of the signals reflected from the scene may, however, cause changes as a function of rotation angle. In this work we explore imaging of simple reflecting targets, which minimizes any potential depolarization. To address this in more complex scene imaging, polarimetric systems may be considered [31].

The transmitters each consisted of a baseband noise sources upconverted to 38 GHz. The output of a 10–1600 MHz noise source was fed to four cascaded wideband amplifiers (Mini-Circuits ZX60-V63+). The amplified noise signal was then inputted to the intermediate frequency (IF) port of the upconverter, which was an Analog Devices GaAs MMIC I/Q upconverter (Analog Devices HMC6787ALC5A). This upconverter was desirable for its integrated frequency doubling feature on the input signal at the local oscillator (LO) port. A 19 GHz LO was used to upconvert the baseband noise signal to the 38 GHz carrier frequency. A power amplifier (Analog Devices HMC7229LS6) was then used to generate a total signal power of 0 dBm which was input to a 10 dBi standard gain horn antenna. Because each noise source ran independently, the noise signals incident on the scene were spatially and temporally incoherent, supporting the use of Fourier-domain image reconstruction. Each receiver consisted of a 15 dBi standard gain horn antenna connected to a 20 dB gain low-noise amplifier (Analog Devices HMC1040LP3CE). The amplified received signal was subsequently routed to a GaAs MMIC I/Q downconverter (Analog Devices HMC6789BLC5A) where the LO was also 19 GHz. The baseband signals were then digitized and recorded using an Agilent MSO-X 92004A oscilloscope at

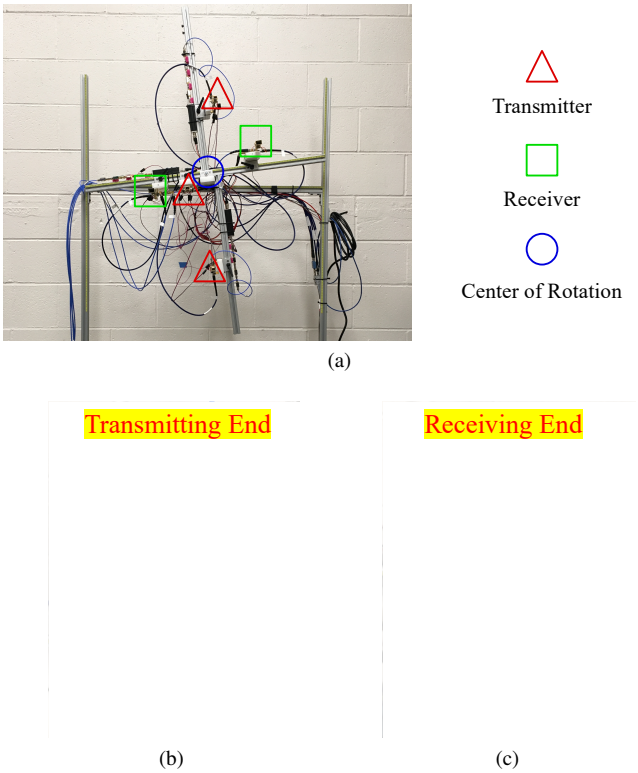

Fig. 6. (a) Photograph of the experimental setup of the proposed dynamic antenna array system. Front view of the implemented dynamic antenna array system with red triangles indicating the location of the transmitters, green squares indicating the location of the receivers, and the blue circle indicating the center of rotation. (b) A close up photograph of one of the transmitters. (c) A close up photograph of one of the receivers.

Fig. 7. Photograph of the experimental setup in a semi-enclosed arch range. The targets consisted of one or two metal reflecting targets.

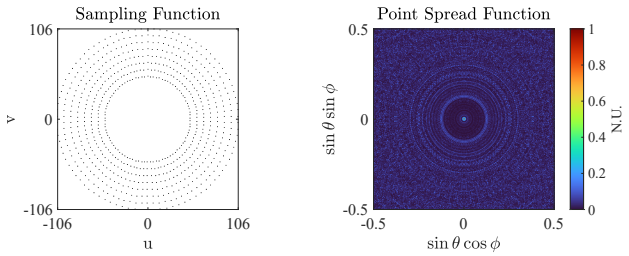

Fig. 8. (a) Synthesized sampling function from the dynamic antenna array setup using 45 angles from 0° to 176° in 4° increment and eight baselines from 50λ to 106λ in 8λ increment. (b) Corresponding point spread function of the synthesized sampling function.

a sampling rate of 2.5 GS/s with an integration time of 100 μs. The data were then processed offline using MATLAB. The LO was generated using an Agilent N5183A signal generator in combination with a four-way splitter (Mini-Circuits ZN4PD1-183W-S+) and a two-way splitter (MIDISCO MDC2288) to provide the five LO signals that were required for the transmitters and receivers.

For the proof-of-concept measurements, the receive antennas were fixed to a given baseline and the structure was rotated. After a single 180° rotation, tracing out one circle in the spatial frequency domain, the receive antennas were relocated to a different baseline and a second spatial frequency circle was measured. This process enabled the synthesis of an equivalent linear receive array using our available hardware resources; a dedicated system with multiple receivers and a multichannel digitizer could also be directly implemented with identical results to those shown herein.

A photograph of the experimental implementation of the dynamic antenna array system is shown in Fig. 6. The implementation supports a 180° rotation, which as described above is sufficient for a full circular sampling function, and supports lateral receive antenna locations within a range of [25λ, 53λ] between each receiving antenna and the center of rotation providing baselines in the range of [50λ, 106λ]. The distance between the center of rotation to the ground is 1.178 m.

V. Experiment

Measurements were conducted in a 7.6m semi-enclosed arch range with microwave absorbers behind the scene of interest (Fig. 7). The targets used in the proof-of-concept measurements were metallic spheres. To align and track the rotation angle of the dynamic antenna, a standard digital angle gauge with 0.1° accuracy was attached to the cross-shaped rotatable frame rail. For rotational motion, 45 angles were used from 0° to 176° in 4° increment where the angle 10° is parallel to the floor. For lateral adjustment to synthesize a sparse linear array, eight selected baselines were considered between the two receiving antennas that were from 50λ to 106λ in 8λ increment. The spatial frequency samples were calculated using the wavelength at the center of the signal bandwidth. The combination between the designed angles and the baselines of the synthesized linear array result in 360 unique spatial Fourier samples for image reconstruction. The simulated sampling function of the experimental system is shown in Fig. 8.

Measurements were conducted for both a single scattering target and two scattering targets. The single scattering target measurement is shown in Fig. 9(a), which considered of a single metallic sphere with a diameter of 24 cm yielding a radar cross-section (RCS) value of -13.4 dBsm at 38 GHz. The metallic sphere was approximately 1.83 m from the

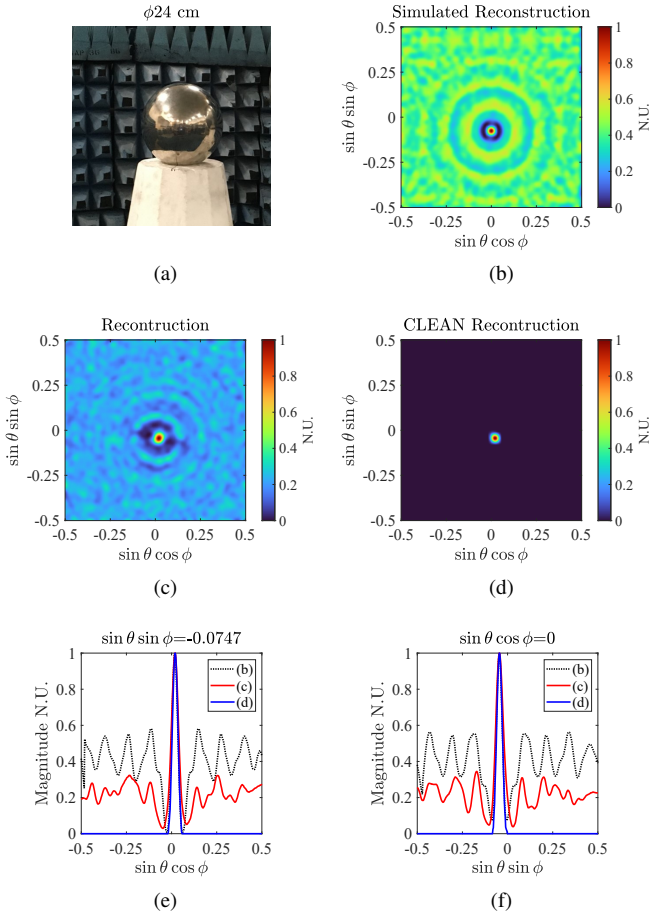

Fig. 9. (a) Scene comprising a single scattering source which is a metallic sphere with a 24 cm diameter and a RCS value of -13.4 dBsm. (b) Simulated reconstruction based on RCS and position. (c) Simple interferometric reconstruction of the measurement on (a). (d) CLEAN deconvolution algorithm [53] applied to (c) using 15 iterations with a loop gain of 1. (e) One dimensional horizontal cut along $\sin\theta\sin\phi = -0.0747$ for comparing the results from (b), (c), and (d). (f) One dimensional vertical cut along $\sin\theta\cos\phi = 0$ for comparing the results in (b), (c), and (d).

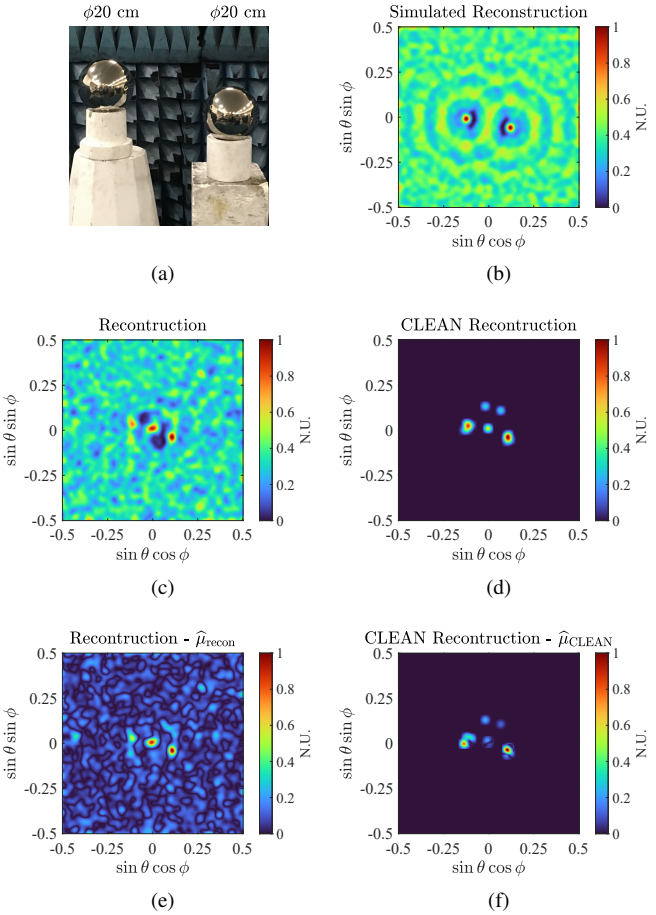

Fig. 10. (a) Scene comprising two scattering sources of equal RCS without RF absorbers in between. Both scattering sources are metallic sphere with a 20 cm diameter yielding a RCS value of -15 dBsm. (b) Simulated reconstruction based on RCS and position of (a). (c) Simple interferometric reconstruction of the measurement on (a). (d) CLEAN deconvolution algorithm [53] applied to (c) using 15 iterations with a loop gain of 1. (e) Further processing on the reconstruction, (c), by removing the mean of the magnitude among all information from the entire reconstructed scene, $\widehat{\mu}_{\text{recon}}$. (f) Further processing on the deconvoluted reconstruction, (d), by removing the mean of the magnitude among all information determined by the CLEAN algorithm, $\widehat{\mu}_{\text{CLEAN}}$. The artifact between the two sphere responses is reduced, and the slight shift in the positions of the responses more closely aligns to the actual locations of the spheres.

dynamic antenna array, had a height of approximately 1.156 m and was positioned to align with the array's center of rotation. A simulated reconstruction using the synthesized sampling function shown in Fig. 8 can be seen in Fig. 9(b). A Gaussian smoothing filter was applied to both simulated and measured image reconstructions. Sidelobe structures can be seen which are due to the radially-discrete nature of the sampling function. The speckles in the image are furthermore a result of the angularly discrete sampling function. The measurement image reconstruction is shown in Fig. 9(c), which matches the simulated reconstruction, along with the sidelobe structure. To refine the image, we implemented the CLEAN algorithm [53] which deconvolves the theoretical point sources responses of the system determined from the simulated sampling function to remove sidelobe artifacts. We implemented the algorithm using 15 iterations with a loop gain value of 1. The computation time of the CLEAN algorithm was approximately 0.1 s on an image of 426×426 pixels, and, being faster than the rotation of the array, is not a limiting factor on the image formation time. The resulting CLEAN image is shown in Fig. 9(d), where the artifacts outside the strong target responses are mitigated. It is evident that the location of the reconstructed scattering source is within close proximity of the actual location as shown in Fig. 9(c) and (d).

The second measured scene shown in Fig. 10(a) comprised two scattering sources of equal RCS without RF absorbents placed between. Both scattering sources were metallic spheres with a 20 cm diameter yielding a RCS value of -15 dBsm. The distance from the dynamic antenna array to the spheres was approximately 1.83 m. The sphere on the left had a height of 1.168 m and the sphere on the right had a height of approximately 1.080 m. The horizontal separation between the two spheres was approximately 0.445 m where the horizontal midpoint between the two spheres was positioned to align with the array's center of rotation. A simulated reconstruction using the synthesized sampling function shown in Fig. 8 can

be seen in Fig. 10(b). The measurement results are shown in Fig. 10(c) and (d) where the former is the direct image reconstruction and the latter is the CLEAN algorithm result. Without deconvolution, it is observed that an unexpected third response appears between the expected locations of the two spheres. Furthermore, the deconvolution reduced but did not eliminate the unexpected response. In spite of this, it is still evident that the locations of the reconstructed scattering sources are within close proximity of the actual locations as shown in Fig. 10(d).

There are a number of possible sources of the unexpected response between the spheres in the reconstructed measurement, including constructive interaction of the sidelobes of the responses of the two targets and multipath scattering in the environment. Two additional measurements based on Fig. 10(a) were conducted attempting to mitigate these factors: the first measurement separated the two spheres at greater distance such that the overlapping sidelobes would be reduced. The second measurement consisted of placing RF absorber between the two spheres to mitigate any multipath effect. Neither approach completely mitigated the artifact, however it is nonetheless possible that one or both of these factors still contribute to the artifact in addition to other factors; further study is warranted. To address the response, we investigated a data-driven correction. In this approach, we subtracted the mean of the reconstructed image $\widehat{\mu}_{\mathrm{recon}}$, which provides a clearer visual contrast as shown in Fig. 10(e) but does not mitigate the response. We also subtracted the mean of the deconvolved image $\widehat{\mu}_{\mathrm{CLEAN}}$, which is the average of the information determined by the CLEAN algorithm. As shown in Fig. 10(f), the unexpected response is significantly mitigated from the reconstruction scene. Furthermore, the responses shift slightly counter-clockwise, which more closely aligns with the actual locations of the two spheres.

VI. Conclusion

In this work, we demonstrated a dynamic antenna array framework for active millimeter-wave imaging applications by implementing rotational dynamics on a sparse linear array. The sampling function of a comparable sparse linear array was synthesized by using two receiving antennas to form multiple baselines which yield a synthesized sampling function over time when incorporated in conjunction with the implemented rotational dynamics. By considering the array dynamics, the number of receiving antennas in the array can be significantly reduced when compared to conventional static interferometric imaging arrays. Furthermore, the use of active noise transmission supports fast rotational dynamics for rapid image formation. Future implementations with receive arrays in uniform linear or minimally-redundant linear array formations may thus support rapid image formation with minimal millimeter-wave hardware, providing a low-cost approach to millimeter-wave imaging for a wide range of remote sensing applications.

This paper presented proof-of-concept experimental demonstrations supporting millimeter-wave imaging with a rotationally dynamic antenna array. Potential future research may focus on improving the image formation quality by using advanced processing techniques, e.g., algorithms adapted to sparse domains, particularly if scenes constructed mainly of a small set of strong scatterers is of interest. Furthermore, while the presented architecture focused on rotational dynamics, it is feasible to envision a system that also incorporates lateral dynamics, by sliding only two antenna elements laterally along the linear array dimension. At the expense of additional measurement time, this approach could obtain significantly more spatial frequency samples, leading to better image reconstruction.

References

[1] N. Currie and C. Brown, *Principles and Applications of Millimeter-Wave Radar*. Artech House, 1987.

[2] J. A. Nanzer, *Microwave and Millimeter-Wave Remote Sensing for Security Applications*. Artech House, 2012.

[3] A. Godavarty, S. Erickson, J. Gonzalez, U. Chaudhary, M. Hall, M. Roman, and R. Roche, "Non-invasive Optical Imaging technology: Breast cancer imaging and functional brain mapping," in *2012 Pan American Health Care Exchanges*, 2012, pp. 125–125.

[4] K. Hossain, C. Mantel, and S. Forchhammer, "Evaluation of Prediction of Quality Metrics for IR Images for UAV Applications," in *2019 Data Compression Conference (DCC)*, 2019, pp. 578–578.

[5] L. C. Graham, "Synthetic interferometer radar for topographic mapping," *Proceedings of the IEEE*, vol. 62, no. 6, pp. 763–768, 1974.

[6] D. Moller, S. Hensley, G. A. Sadowy, C. D. Fisher, T. Michel, M. Zawadzki, and E. Rignot, "The Glacier and Land Ice Surface Topography Interferometer: An Airborne Proof-of-Concept Demonstration of High-Precision Ka-Band Single-Pass Elevation Mapping," *IEEE Trans. Geosci. Remote Sens.*, vol. 49, no. 2, pp. 827–842, 2011.

[7] R. Seu, S. Smrekar, S. Hensley, and P. Lombardo, "A SAR Interferometer Experiment to Explore the Surface of Venus," in *Proceedings of EUSAR 2016: 11th European Conference on Synthetic Aperture Radar*, 2016, pp. 1–3.

[8] F. Gumbmann and L. Schmidt, "Millimeter-Wave Imaging With Optimized Sparse Periodic Array for Short-Range Applications," *IEEE Trans. Geosci. Remote Sens.*, vol. 49, no. 10, pp. 3629–3638, 2011.

[9] E. C. Fear, X. Li, S. C. Hagness, and M. A. Stuchly, "Confocal microwave imaging for breast cancer detection: localization of tumors in three dimensions," *IEEE Transactions on Biomedical Engineering*, vol. 49, no. 8, pp. 812–822, 2002.

[10] D. M. Sheen, D. L. McMakin, and T. E. Hall, "Three-dimensional millimeter-wave imaging for concealed weapon detection," *IEEE Trans. Microw. Theory Techn.*, vol. 49, no. 9, pp. 1581–1592, 2001.

[11] J. P. P. Gomes, J. F. B. Brancalion, and D. Fernandes, "Automatic Target Recognition in Synthetic Aperture Radar image using multiresolution analysis and classifiers combination," in *2008 IEEE Radar Conference*, 2008, pp. 1–5.

[12] U. Srinivas, V. Monga, and R. G. Raj, "SAR Automatic Target Recognition Using Discriminative Graphical Models," *IEEE Trans. Aerosp. Electron. Syst.*, vol. 50, no. 1, pp. 591–606, Jan. 2014.

[13] S. Stanko, D. Notel, A. Wahlen, J. Huck, F. Kloppel, R. Sommer, M. Hagelen, and H. Essen, "Active and passive mm-wave imaging for concealed weapon detection and surveillance," in *2008 33rd International Conference on Infrared, Millimeter and Terahertz Waves*, 2008, pp. 1–2.

[14] C. Zheng, X. Yao, A. Hu, and J. Miao, "A Passive Millimeter-Wave Imager Used For Concealed Weapon Detection," *Progress In Electromagnetics Research B*, vol. 46, p. 379–397, 2013.

[15] M. F. Imani, J. N. Gollub, O. Yurduseven, A. V. Diebold, M. Boyarsky, T. Fromenteze, L. Pulido-Mancera, T. Sleasman, and D. R. Smith, "Review of Metasurface Antennas for Computational Microwave Imaging," *IEEE Trans. Antennas Propag.*, vol. 68, no. 3, pp. 1860–1875, 2020.

[16] T. Sleasman, M. Boyarsky, L. Pulido-Mancera, T. Fromenteze, M. F. Imani, M. S. Reynolds, and D. R. Smith, "Experimental Synthetic Aperture Radar With Dynamic Metasurfaces," *IEEE Trans. Antennas Propag.*, vol. 65, no. 12, pp. 6864–6877, 2017.

[17] L. M. Neira, B. D. Van Veen, and S. C. Hagness, "High-Resolution Microwave Breast Imaging Using a 3-D Inverse Scattering Algorithm With a Variable-Strength Spatial Prior Constraint," *IEEE Trans. Antennas Propag.*, vol. 65, no. 11, pp. 6002–6014, 2017.

[18] A. R. Thompson, J. M. Moran, and G. W. Swenson, *Interferometry and Synthesis in Radio Astronomy*. John Wiley and Sons, 2001.

[19] J. A. Nanzer, "Millimeter-wave interferometric imaging sensors," in *SENSORS, 2013 IEEE*, Nov 2013, pp. 1–4.

[20] A. Ferretti, C. Prati, and F. Rocca, "Permanent scatterers in SAR interferometry," *IEEE Trans. Geosci. Remote Sens.*, vol. 39, no. 1, pp. 8–20, 2001.

[21] K. Schulz, D. Brunner, and M. Boldt, "Comparison of CoVAmCoh and ILU image products for interferometric very high resolution SAR image pairs," in *2011 IEEE International Geoscience and Remote Sensing Symposium*, 2011, pp. 313–315.

[22] Y. Álvarez, Y. Rodriguez-Vaqueiro, B. Gonzalez-Valdes, F. Las-Heras, and A. García-Pino, "Fourier-Based Imaging for Subsampled Multistatic Arrays," *IEEE Trans. Antennas Propag.*, vol. 64, no. 6, pp. 2557–2562, Jun. 2016.

[23] D. Soncco, C. Barbanson, M. Nikolova, A. Almansa, and Y. Ferrec, "Fast and Accurate Multiplicative Decomposition for Fringe Removal in Interferometric Images," *IEEE Trans. Comput. Imaging*, vol. 3, no. 2, pp. 187–201, Jun. 2017.

[24] E. Kpré, C. Decroze, M. Mouhamadou, and T. Fromenteze, "Computational Imaging for Compressive Synthetic Aperture Interferometric Radiometer," *IEEE Trans. Antennas Propag.*, vol. 66, no. 10, pp. 5546–5557, Oct. 2018.

[25] D. Chen, S. Vakalis, and J. A. Nanzer, "Dynamic Antenna Array Design for Scene Classification Through Fourier-Domain Filtering," *IEEE Trans. Antennas Propag.*, vol. 69, no. 9, pp. 5953–5962, Sep. 2021.

[26] ——, "A Millimeter-Wave Dynamic Antenna Array for Classifying Objects Via Sparse Fourier Domain Sampling," in *2021 IEEE MTT-S International Microwave Symposium (IMS)*, 2021, pp. 748–751.

[27] D. Chen, S. Vakalis, V. Holmes, and J. A. Nanzer, "Spatial Frequency Filter Design for Interferometric Image Classification Without Image Reconstruction," in *2020 IEEE USNC-CNC-URSI North American Radio Science Meeting (Joint with AP-S Symposium)*, 2020, pp. 23–24.

[28] S. Vakalis and J. A. Nanzer, "Microwave Imaging Using Noise Signals," *IEEE Trans. Microw. Theory Techn.*, vol. 66, no. 12, pp. 5842–5851, Dec. 2018.

[29] S. Vakalis, L. Gong, Y. He, J. Papapolymerou, and J. A. Nanzer, "Experimental Demonstration and Calibration of a 16-Element Active Incoherent Millimeter-Wave Imaging Array," *IEEE Trans. Microw. Theory Techn.*, vol. 68, no. 9, pp. 3804–3813, Sep. 2020.

[30] S. Vakalis, L. Gong, and J. A. Nanzer, "Imaging With WiFi," *IEEE Access*, vol. 7, pp. 28 616–28 624, 2019.

[31] J. Wang, P. Aubry, and A. Yarovoy, "A Novel Rotated Antenna Array Topology for Near-Field 3-D Fully Polarimetric Imaging," *IEEE Transactions on Antennas and Propagation*, vol. 66, no. 3, pp. 1584–1589, 2018.

[32] P. C. Theofanopoulos, M. Sakr, and G. C. Trichopoulos, "Multistatic Terahertz Imaging Using the Radon Transform," *IEEE Trans. Antennas Propag.*, vol. 67, no. 4, pp. 2700–2709, 2019.

[33] M. Pieraccini, F. Papi, and S. Rocchio, "Interferometric RotoSAR," *Electronics Letters*, vol. 51, no. 18, pp. 1451–1453, Sep. 2015. [Online]. Available: https://doi.org/10.1049/el.2015.1785

[34] C. S. Ruf, C. T. Swift, A. B. Tanner, and D. M. Le Vine, "Interferometric synthetic aperture microwave radiometry for the remote sensing of the Earth," *IEEE Trans. Geosci. Remote Sens.*, vol. 26, no. 5, pp. 597–611, Sep. 1988.

[35] K. van 't Klooster, "A few examples of interferometry applications in space-related active and passive remote sensing," in *2004 Second International Workshop Ultrawideband and Ultrashort Impulse Signals (IEEE Cat. No.04EX925)*, 2004, pp. 55–58.

[36] T. Amiot, F. Douchin, E. Thouvenot, J. C. Souyris, and B. Cugny, "The interferometric cartwheel: a multi-purpose formation of passive radar microsatellites," in *IEEE International Geoscience and Remote Sensing Symposium*, vol. 1, 2002, pp. 435–437 vol.1.

[37] P. Bei and W. Ji, "2-D Frequency Spectrum Features and Error Analysis for Interferometric Passive Microwave Imager," in *2007 International Symposium on Microwave, Antenna, Propagation and EMC Technologies for Wireless Communications*, 2007, pp. 1454–1457.

[38] A. V. Diebold, M. F. Imani, T. Fromenteze, D. L. Marks, and D. R. Smith, "Passive microwave spectral imaging with dynamic metasurface apertures," *Optica*, vol. 7, no. 5, pp. 527–536, May 2020. [Online]. Available: http://www.osapublishing.org/optica/abstract.cfm?URI=optica-7-5-527

[39] M. Born, E. Wolf, A. B. Bhatia, P. C. Clemmow, D. Gabor, A. R. Stokes, A. M. Taylor, P. A. Wayman, and W. L. Wilcock, *Principles of Optics: Electromagnetic Theory of Propagation, Interference and Diffraction of Light*, 7th ed. Cambridge University Press, 1999.

[40] S. Vakalis and J. A. Nanzer, "An information-theoretic approach to waveform design for active incoherent microwave imaging," in *2018 IEEE Conference on Antenna Measurements Applications (CAMA)*, 2018, pp. 1–4.

[41] ——, "Transmit pattern analysis for active incoherent microwave imaging," in *2019 IEEE International Symposium on Antennas and Propagation and USNC-URSI Radio Science Meeting*, 2019, pp. 813–814.

[42] ——, "Distributed array transmitter spatial coherence in active incoherent millimeter-wave imaging," in *2020 IEEE International Symposium on Antennas and Propagation and North American Radio Science Meeting*, 2020, pp. 1169–1170.

[43] ——, "Impact of time-bandwidth product on active incoherent millimeter-wave imaging," in *2021 IEEE International Symposium on Antennas and Propagation and USNC-URSI Radio Science Meeting (APS/URSI)*, 2021, pp. 1835–1836.

[44] S. Vakalis, D. Chen, and J. A. Nanzer, "Toward space–time incoherent transmitter design for millimeter-wave imaging," *IEEE Antennas and Wireless Propagation Letters*, vol. 19, no. 9, pp. 1471–1475, 2020.

[45] S. Vakalis, S. Mghabghab, and J. A. Nanzer, "Passive non-cooperative millimeter-wave imaging using 5g signals of opportunity," in *2021 IEEE MTT-S International Microwave Symposium (IMS)*, 2021, pp. 549–552.

[46] S. Vakalis and J. A. Nanzer, "The Near Field Effect in Transmitter Design for Incoherent Millimeter-Wave Imaging," in *2021 XXXIVth General Assembly and Scientific Symposium of the International Union of Radio Science (URSI GASS)*, 2021, pp. 01–04.

[47] N. A. Salmon, R. Macpherson, A. Harvey, P. Hall, S. Hayward, P. Wilkinson, and C. Taylor, "First video rate imagery from a 32-channel 22-GHz aperture synthesis passive millimetre wave imager," *Proc.SPIE*, vol. 8188, 2011.

[48] J. A. Nanzer and R. L. Rogers, "A Ka-band Correlation Radiometer for Human Presence Detection from a Moving Platform," in *2007 IEEE/MTT-S International Microwave Symposium*, 2007, pp. 385–388.

[49] A. Moffet, "Minimum-redundancy linear arrays," *IEEE Trans. Antennas Propag.*, vol. 16, no. 2, pp. 172–175, 1968.

[50] Z. Wang, A. Bovik, H. Sheikh, and E. Simoncelli, "Image quality assessment: from error visibility to structural similarity," *IEEE Transactions on Image Processing*, vol. 13, no. 4, pp. 600–612, 2004.

[51] S. Vakalis, D. Chen, and J. A. Nanzer, "Millimeter-Wave Imaging at 652 Frames per Second," *IEEE Journal of Microwaves*, pp. 1–9, 2021.

[52] C. Balanis, *Antenna theory: analysis and design*. Wiley-Interscience, 2016.

[53] J. A. Hogbom, "Aperture Synthesis with a Non-Regular Distribution of Interferometer Baselines," *Astron. Astrophys. Suppl. Ser.*, vol. 15, pp. 417–426, 1974.